Transition-Metal-Free Magnesium-Based Batteries Activated by Anionic Insertion into Fluorinated Graphene Nanosheets

Junjie Xie, Chilin Li, Zhonghui Cui, and Xiangxin Guo*

Considering resource abundance, high volumetric energy density, and safer anodic electroplating, the Mg-based battery is thought to be one of the most promising systems beyond current Li-ion batteries. However, the development of Mg batteries is hindered by the narrow electrochemical window of electrolytes as well as by inapplicable cathode frameworks. In this work, it is proposed, for the first time, to utilize a fast surface redox process to replace sluggish lattice migration for improving the kinetics of Mg batteries. Taking fluorinated graphene nanosheets (FGSs) as model material, a reversible capacity higher than 100 mAh g^{-1} is achieved in a pseudocapacitance behavior from 2.75 to 0.5 V. Different from traditional storage mechanisms, this proof-of-concept Mg/FGS system is activated by a prior anionic process followed by reversible cationic storage. The dilution of charge density by forming large-sized monovalent complex cations and the easy access to surface redox sites are responsible for the negligible voltage polarization without an evident MgF$_2$ nucleation phenomenon.

1. Introduction

Recently, the interests in developing advanced energy storage systems are rapidly boosted by the requirements on large-scale stationary electric-grid and plug-in hybrid electric vehicles. Therein safety and cost control are pushed to more important status. Because of an abundant reserve of multivalent elements (e.g., Mg, Al, and Ca) and their suppressed dendrite growth, the corresponding multivalent batteries are thought to be potential candidates beyond current Li-ion batteries (LIBs).[1] Furthermore compared with Li metal, multivalent metals have higher volumetric capacity (e.g., 3833 mAh cm^{-3} for Mg vs 2205 mAh cm^{-3} for Li).[2] Considering the similar ionic radius of Mg^{2+} (0.86 Å) as that of Li^{+} (0.9 Å), Mg batteries are expected to have comparable energy or power density as that of LIBs even though the reduction potential of Mg^{2+}/Mg (–2.4 V vs standard hydrogen electrode) is 0.6 V higher than that of Li^{+}/Li.[1] Unfortunately, the double charge density causes a serious slowing down of Mg^{2+} solid-state diffusion or irreversible cation trapping in many crystal structures including open frameworks.[3,4] The lack of electrolytes with wide electrochemical window also retards us to explore more high-voltage host structures.[5] Moreover, the passivation layer easily formed on Mg anode is not always permeable for reversible Mg plating/stripping as opposed to the solid–electrolyte interface (SEI) at Li anode.[6] These prevent the development of Mg batteries based on rocking chair–type shuttle of single divalent cation with high polarity.

Two alternative technologies still based on Mg anode have been proposed in order to circumvent sluggish Mg^{2+} insertion at cathode. One is the Mg/Li hybrid battery (MLB),[7] where Li^{+} instead of Mg^{2+} is preferentially inserted into cathode host and as a consequence the choice range of cathode materials is greatly extended. However, the present Mg/Li dual-salt electrolytes usually contain borohydrides or chlorides and their upper voltage windows are limited (<2 V). Therefore, many structure prototypes (e.g., spinel, olivine) or electrochemical reaction occurring at higher voltage are still not utilizable.[5] The other hybrid system is to achieve reversible anionic insertion at cathode, and is expected to possess higher reaction voltage as indicated by an early prototype "dual-graphite cell," which can release most of capacity in a voltage range of 4.5–5.0 V.[8] Most recently, anionic insertion cells based on Mg anode were reported by Zhang and Zhao et al.[9] However, the dominant anionic carrier (e.g., chloride ions) is highly corrosive, and the host frameworks (e.g., transition metal oxychlorides) are heavy in weight, leading to a poor capacity release and preservation (<80 mAh g^{-1}).

Apart from as supporter for anionic insertion or adsorption, more usually functionalized carbon-based materials provide redox sites for monovalent cations (e.g., Li^{+}, Na^{+}).[10] Mobile cations are generally of smaller size and less corrosivity than anions, therefore resulting in better capacity/rate performance or pseudocapacitive behavior especially when resorting to surface-decorated graphene derivates with 3D pore channels.[10c] Fluorinated graphites (CF$_x$) have been proved to be rechargeable when coupled with Mg anode.[11] Its reaction mechanism was thought to be associated with the formation/breaking of

Dr. J. Xie, Prof. C. Li, Dr. Z. Cui, Prof. X. Guo
State Key Laboratory of High Performance
Ceramics and Superfine Microstructure
Shanghai Institute of Ceramics
Chinese Academy of Sciences
1295 Ding Xi Road, Shanghai 200050, China
E-mail: chilinli@mail.sic.ac.cn

DOI: 10.1002/adfm.201503010

Mg—F bonds, but the exact details are still unclear. The observed large polarization likely stems from high insulativity due to rich F content during harsh gas fluorination process, as well as difficult access of Mg^{2+} to interlayer of graphite. It may also suffer from remarkable volume change if larger sized cation/anion complex insertion is involved. In order to improve polarization, we require to decrease F content (i.e., increase intrinsic conductivity) by mild fluorination and meantime expand graphite into few-layer graphene with higher surface area and more exposed redox sites. In this work, for the first time we achieve a reversible Mg-ion shuttle between the cathode of fluorinated graphene nanosheet (FGS) network and Mg anode after a prior activation by anionic insertion into cathode. This new proof-of-concept Mg-based system has several advantages. 1) It bypasses the use of transition metal contained crystalline structure and avoids sluggish lattice-associated transport of Mg. It utilizes graphene-like surfaces full of desired functional groups as exposed redox sites to accommodate facile Mg^{2+} adsorption with a pseudocapacitive behavior and more symmetric discharge/charge curves. 2) In this system, the use of complex and expensive Grignard reagents is avoided. Instead, we use more common $Mg(ClO_4)_2$ and dimethyl sulfoxide (DMSO) as electrolyte components. DMSO is expected to have strong dissolution capability toward Mg salt and is in favor for the preparation of high-concentration Mg electrolyte. A complicated reaction mechanism referring to anionic insertion during the first charge and cationic shuttle during the following cycles is discussed for Mg/FGS batteries.

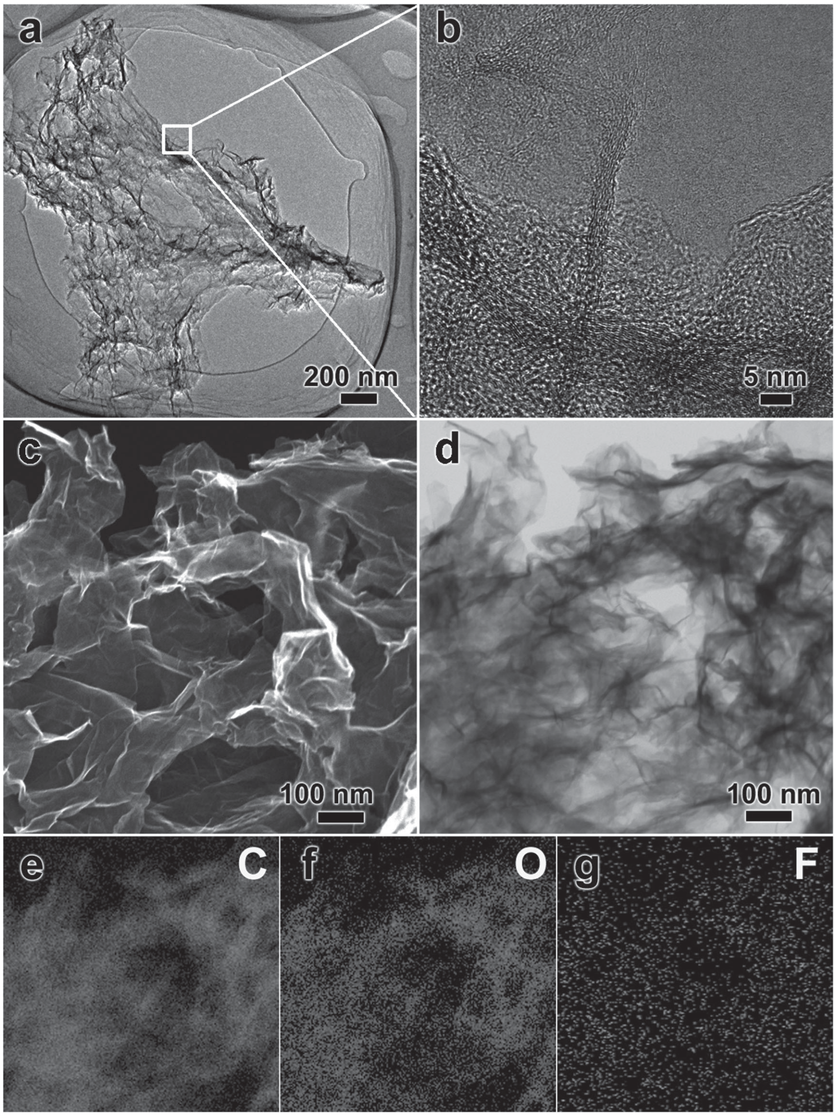

Figure 1. a) TEM image of a typical area of porous FGS. b) Enlarged TEM image of FGS showing a typical thickness of around 4 nm. c) High-angle annular dark-field and d) bright-field STEM images of the porous structure of 3D self-assembled FGS. The corresponding EDX mapping images of e) C, f) O, and g) F elements in FGS. Homogenous distributions of oxygen and fluorine components confirm that fluorination takes effect and F atoms are uniformly bonded with the carbon framework, where O is still residual.

2. Results and Discussion

Since exfoliation of fluorinated graphite or fluorination of graphene sheets (GS) is difficult or energy-consuming, we resort to fluorinate graphene oxide (GO) to construct 3D self-assembled network of FGS. GO is expected to have higher surface activity than GS. Hydrothermal fluorination in this work simultaneously leads to partial removal of oxygen-contained functional groups and surface fluorination by hydrofluoric acid (HF).[12] The residual of oxygenated functional groups on surface is helpful to prevent a serious restacking of FGSs.[13] The capsulated water molecules are in favor to shape the self-assembly of FGSs, and they can be finally removed during freeze-drying. The typical 3D porous morphology of FGSs is shown in transmission electron microscope (TEM) images and scanning TEM (STEM) mapping of **Figure 1**. Similar to 2D wrinkled sheet-like structure, the FGSs are stable and transparent under electron beam irradiation with a typical thickness around 4 nm as observed in high-resolution TEM (HRTEM, Figure 1b), indicating that FGSs consist of 4–5 layers. Homogenous distribution of carbon, oxygen, and fluorine components in FGSs is verified by element mapping as shown in Figure 1e–g, confirming that fluorination takes effect and F atoms are uniformly bonded with carbon framework.

The structural and bonding characteristics of FGSs by reducing and fluorinating GO are elucidated by power X-ray diffraction (XRD) patterns and X-ray photoelectron spectra (XPS) as shown in **Figure 2**. GO displays a characteristic XRD peak at 12° with a *d*-spacing of 0.74 nm as a consequence of insertion of a substantial amount of oxygen atoms into graphite interlayer. Without the addition of fluorinating agent (e.g., HF),

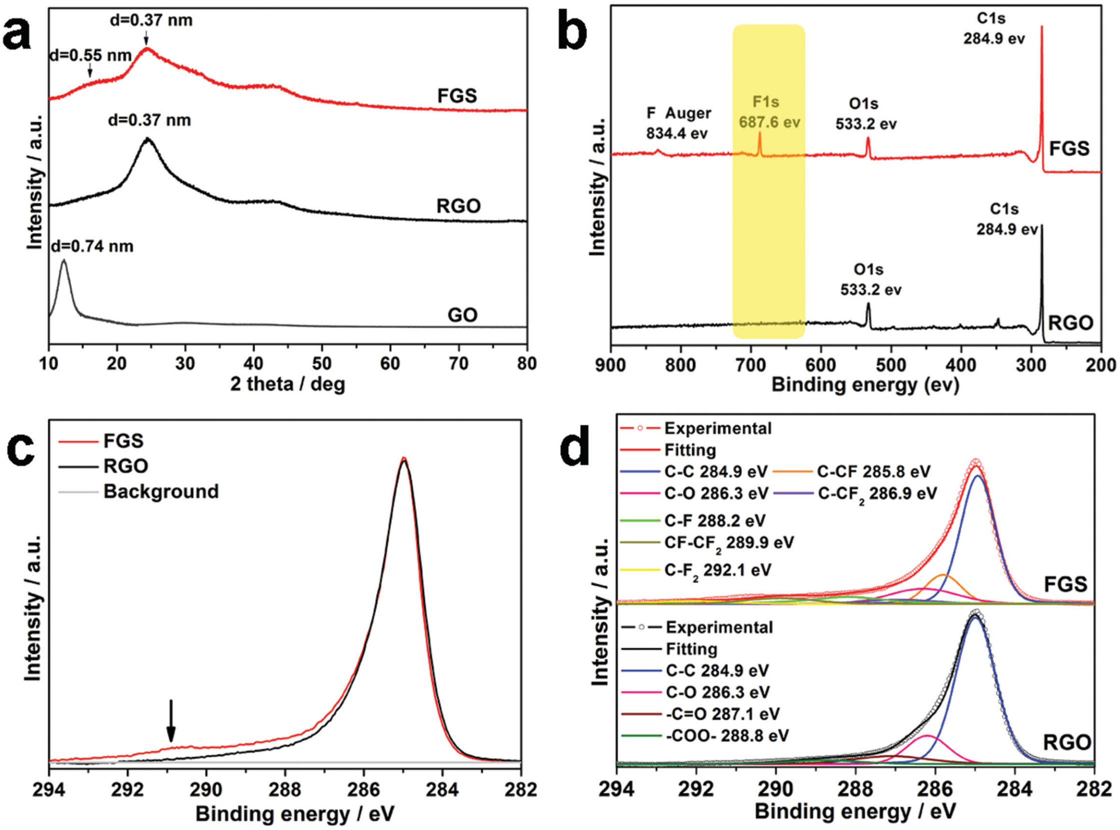

Figure 2. a) Power XRD patterns of FGS, RGO, and GO with different *d*-spacing values. b) Overview XPS spectra of FGS and RGO with peak signals of C 1s, O 1s, and F 1s. Remarkable F signals are exclusively observed in FGS after hydrothermal fluorination. c) Comparison of C 1s peaks between FGS and RGO after normalization. d) Gaussian fitting and deconvoluted peak assignment of C 1s spectra of FGS and RGO.

GO is converted into reduced graphene oxide (RGO) by the similar hydrothermal method.[13] The main XRD peaks of RGO and FGS are shifted to a higher angle around 24° with much broader profiles, indicating a *d*-spacing of 0.37 nm for both RGO and FGS. This value is comparable with that of graphite (0.34 nm), confirming a substantial deoxygenation from GO.[12] For FGSs, one can also note an additional broad peak appearing at around 16° with a *d*-spacing of 0.55 nm. It could be indexed as the (001) or (002) reflection in a hexagonal structure, corresponding to a typical stage 1 intercalation of CF_x.[14]

To eliminate the interference of residual HF toward the F-bonding information, the FGS samples were washed by deionized water with several times until the pH value is neutral. Overview of XPS comparison of FGS with RGO discloses a substantial existence of F 1s peak at 687.6 eV for the former, denoting the formation of C—F covalent bonding after hydrothermal fluorination (Figure 2b).[12] The relative atomic content of C to F ($R_{C/F}$) for FGS is estimated to be 9.72, and the relative contents of C to O ($R_{C/O}$) for RGO (8.13) and FGS (8.57) are almost same (Table S1, Supporting Information). It means that fluorination does not cause a more in-depth deoxygenation and some oxygenated functional groups of GO are difficult to be removed during relatively mild hydrothermal reaction. The fluorination effect is also detected from the normalized C 1s spectra of RGO and FGS, where the latter curve shows higher intensity at the binding energies (>287 eV) associated with various C—F or C—CF_x bonds (Figure 2c). Their detailed assignment of convoluted XPS peaks is shown in Figure 2d. Both the samples display the common C 1s signals containing C—C (284.9 eV) and C—O (286.3 eV). Compared with RGO, the additional C 1s peaks of FGS are, respectively, assigned to C—CF (285.8 eV), C—CF_2 (286.9 eV), C—F (288.2 eV), CF—CF_2 (289.9 eV), and C—F_2 (292.1 eV).[12] The C 1s spectrum of RGO also shows residual oxygenation characteristic peaks of very weak intensity, such as —C=O (287.1 eV) and —COO— (288.8 eV), which confirms an effective reduction of GO during hydrothermal process. These peaks are further suppressed during fluorination in view of a potential substitution of O by F atoms in —C=O and —COO— sites.[12] Raman spectra show that the intensity ratio of D and G peaks (I_D/I_G) for FGS (1.06) is similar to that for RGO (1.07) (Figure S1, Supporting Information), indicating that fluorination does not significantly influence the order degree of carbon.

The galvanostatic charge–discharge curves and cycling number of Mg/FGS batteries are shown in **Figure 3**. During the first cycle, the discharge process is performed prior to the charge one (Figure 3a). Unexpectedly, the initial discharge capacity is negligible (≈25 mAh g^{-1}) and instead a much higher capacity exceeding 200 mAh g^{-1} is achieved during the first charge process. It indicates an unusual anionic intercalation characterized by a slope curve raising from 0.5 to 2.5 V with a capacity of 100 mAh g^{-1}, which is followed by a quasi-plateau

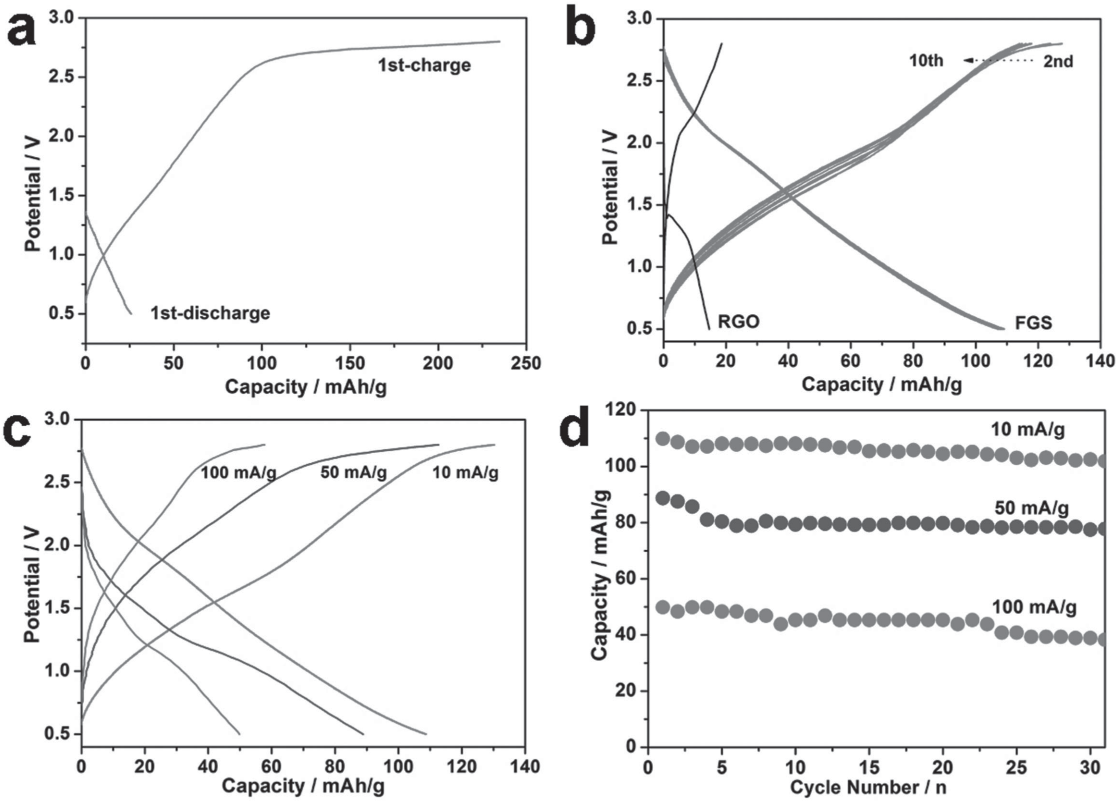

Figure 3. a) Galvanostatic charge–discharge curves of a Mg/FGS battery during the first cycle at 10 mA g^{-1}. The discharge is performed prior to the charge process. b) Following charge–discharge curves of Mg/FGS from the second to tenth cycle after the initial anionic activation. The curves of Mg/RGO are also listed as a comparison. c) Rate and d) cycle performance of Mg/FGS after anionic activation at different current densities from 10 to 100 mA g^{-1}. Mg/FGS batteries show symmetric charge–discharge processes with high reversibility, pseudocapacitive-like profiles, and negligible voltage polarization.

region up to 2.75 V with a capacity of 130 mAh g^{-1}. In fact, the following electrochemistry behavior does not depend on the initial discharge or charge. Even without a prior discharge process, the initial charge displays the similar voltage profile and capacity. Note that if the upper cut-off voltage is limited to 2.5 V, the reversible capacity is as low as 40–50 mAh g^{-1} at 10 mA g^{-1} during the early cycles (Figure S2, Supporting Information). The plateau-like charging up to 2.75 V unlikely corresponds to electrolyte decomposition, since this electrolyte has been reported to be tolerable up to at least 3 V even in oxygen ambience and at enhanced temperature.[15] This anionic storage activates the following cycling with a highly reversible capacity of 110 mAh g^{-1} at 10 mA g^{-1} within 10 cycles (Figure 3b) and of 100 mAh g^{-1} within 30 cycles (Figure 3d). When increasing the current density to 50 and 100 mA g^{-1}, the reversible capacities are still as high as 90 and 50 mAh g^{-1} and are preserved at 80 and 40 mAh g^{-1} after 30 cycles, respectively (Figure 3c,d). The advantages of our FGSs over already reported fluorinated graphites lie in the much more symmetric charge–discharge curves with pseudocapacitive-like profiles and negligible voltage polarization.[11] In our case, the redox active F sites are exposed at the surface of carbonaceous nanosheets, which serve as both the conductive support and electrolyte-permeable porous framework. It circumvents the requirement on Mg migration into fluorinated interlayers of graphite as bulk redox sites with high diffusion barrier. Therefore, the combination of accessible redox sites and mixed conductive network endows FGS with satisfactory electrochemistry even for multivalent ion storage. Note that the reversible capacity of Mg/RGO is as low as 18 mAh g^{-1} with large voltage polarization (Figure 3b). It indicates that the oxygenation groups (at least the dominant C—O group) are not favorable for bonding with Mg or ClO$_4^-$ anion, although they have been demonstrated to enable a release of substantial reversible capacity when bonding with monovalent cation (e.g., Li$^+$ or Na$^+$).[10b,c]

So far, it is still unclear whether the following capacity in Mg/FGS stems from reversible anionic or cationic shuttle after activation by the first anionic intercalation. XPS and STEM are used to analyze the evolution of surface bondings and components at different cycling stages in order to disclose the reaction mechanism. The signal of Mg 1s XPS peak (at 1304.5 eV) is detectable from **Figure** 4b even in the first charged sample with dominant anionic intercalation. It is still unclear whether the Mg-contained anion exists or charging process leads to the formation of Mg-contained SEI. But the latter possibility is implied by the weakening of F 1s peak intensity as well as the appearance of a very weak Mg—F bonding peak (at 686 eV) compared with the pristine sample (Figure 4a).[16] To rule out the interference of poly(vinylidene fluoride) (PVDF) binder, F-free sodium alginate (SA) was used as binder. The ClO$_4^-$-based

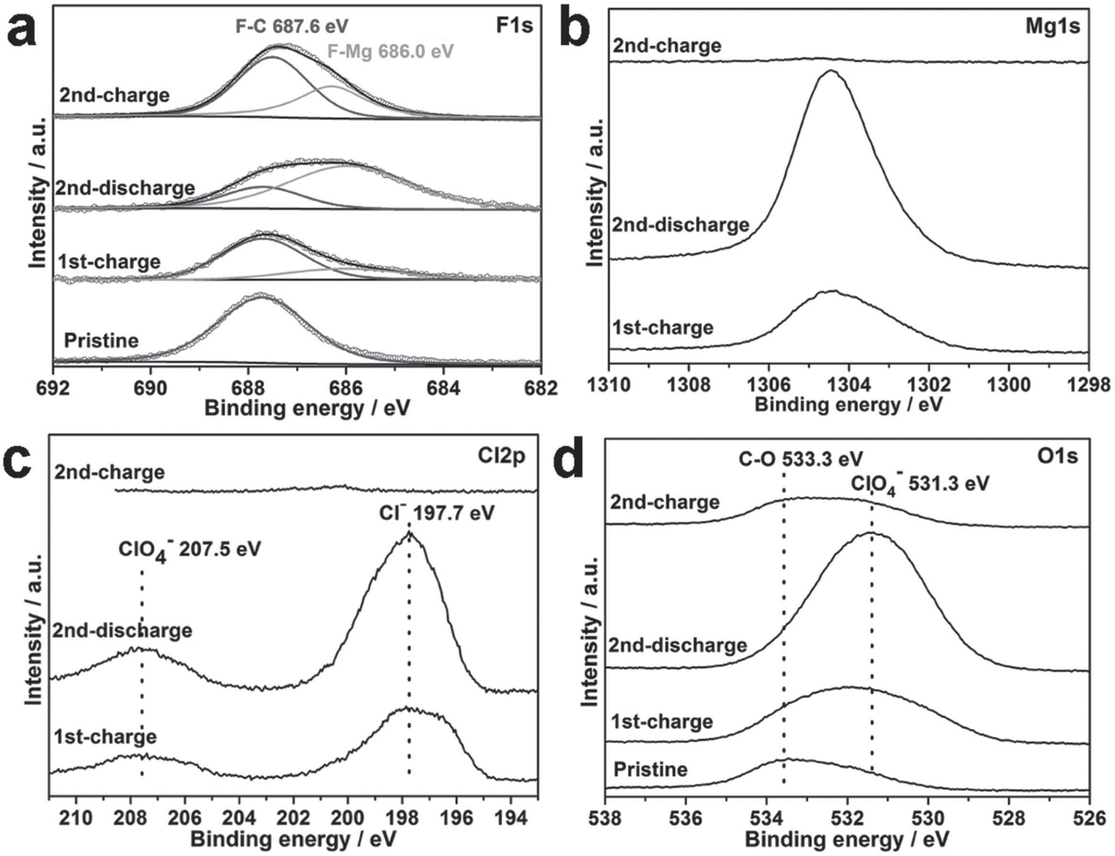

Figure 4. XPS spectra of a) F 1s, b) Mg 1s, c) Cl 2p, and d) O 1s for pristine, first charged, second discharged, and second charged FGS samples. Mg 1s can be detected in the form of a Mg—F bond and a Mg—ClO$_4$ or Mg—Cl interaction, which become more pronounced during the second discharge than during the first charge, and are weakened again during the second charge. The adsorbed ClO$_4^-$ groups likely convert to Cl$^-$ groups according to the Cl 2p spectra evolution. Both ClO$_4^-$ and Cl$^-$ signals are removable after the second charge.

anion insertion during the first charge is confirmed by the observation of Cl 2p peaks as well as O 1s signal toward lower binding energy around 531.3 eV,[17] compared with the pristine sample with a wide O 1s signal of C—O bonding around 533.3 eV (Figure 4c,d). Unexpectedly, although the Cl 2p peak denoting perchlorate (ClO$_4^-$) is observable around 207.5 eV, the peak around 197.7 eV is more remarkable and therefore indicative of a dominant presence of chloride (Cl$^-$).[18] The reductive decomposition from ClO$_4^-$ to Cl$^-$ is possible in nonaqueous medium under the existence of an electron donor.[19] In our case both the DMSO molecule and carbon framework can serve as potential electron donors to promote such conversion at electrode surface.[20] Figure S3 (Supporting Information) compares the XPS peaks of Cl 2p and O 1s between the samples after the initial discharge and charge. Different from the case of first charge, we cannot observe remarkable Cl 2p signal as well as O 1s signal belonging to ClO$_4^-$. It indicates a negligible insertion of ClO$_4^-$ during the initial discharge and that the Cl 2p signal indeed stems from the first charge rather than the Cl residual after the initial discharge.

Therefore, for the following cycling it is difficult to perform a reversible ClO$_4^-$ based shuttle due to a facile decomposition of ClO$_4^-$ carriers. Instead, we find much more intensified Mg1s and F 1s signals referring to Mg—F bonding in the discharged sample after activation. For F 1s spectra, the peak area ratio of Mg—F in the sum of Mg—F (686.0 eV) and C—F (687.6 eV) increases significantly from 26.5% to 75.7% (Figure S4, Supporting Information). More Mg inclusion in cathode after second discharge indicates a potential change of reaction mechanism from anionic insertion to cationic insertion. In view of high polarity and charge density of Mg^{2+}, it is prone to form larger sized complex carrier with surrounding ions and molecules in electrolyte, such as Mg(DMSO)$_n^{2+}$ and Mg(DMSO)$_n$ClO$_4^+$.[21] Further strengthened O 1s (at 531.3 eV) and Cl 2p signals (at 207.5 and 197.7 eV) indicate the presence and intercalation of the latter complex cation, since they are impossible to stem from anionic insertion of ClO$_4^-$ or Cl$^-$ during discharge. A substantial conversion to Cl$^-$ is likely responsible for the adsorption of a large amount of Mg^{2+} to the negatively charged electrode surface. Since Mg^{2+} moves in a form of complex, its storage inevitably brings about more ClO$_4^-$ adsorption as confirmed by the more intensified O 1s and Cl 2p peaks in the second discharged sample than in the first charged sample. The decomposition of ClO$_4^-$ is not halted during the second discharge, therefore leading to a sharper Cl 2p peak belonging to Cl$^-$.

After the second charge, the XPS signals of Mg 1s and Cl 2p are very weak and Mg-based complex cations are expected

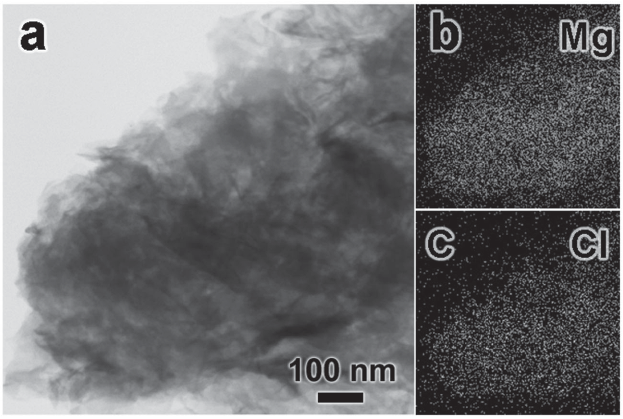

Figure 5. a) Bright field STEM image and b,c) corresponding element mapping of Mg and Cl of a FGS sample after the second discharge. This further confirms the presence and uniform distribution of Mg and Cl components in the second discharged sample.

to desorb from FGS framework. A substantial weakening of Cl^- signal at 197.7 eV indicates that the mobile cations likely contain $MgCl^+$ or $Mg_2Cl_3^+$.[1,2,9a] Correspondingly, the main peak of O 1s is significantly weakened and shifts back to the position of pristine sample. In contrast to the O 1s, Mg 1s, and Cl 2p spectra, the F 1s spectrum becomes intensive again but with a smaller fraction of Mg—F component due to removal of Mg-based carriers and SEI (Figure S4, Supporting Information). C 1s spectra show the similar tendency of peak intensity evolution as F 1s (Figure S5, Supporting Information). Table S2 (Supporting Information) summarizes the atom ratio of all the elements in FGS frameworks at different cycling stages by XPS analysis. Note that the residual of solvent DMSO is negligible in all the samples, indicating DMSO is dissociated from the Mg^{2+}-based complex cations when bonding of these solvates with surface function groups of FGS.[10] STEM mapping further confirms the presence of Mg and Cl components in the second discharged sample (**Figure 5**). This result is in good agreement with the XPS analysis.

The scheme of **Figure 6** depicts the detailed electrochemical mechanisms involving multiple (complex) cation or anion (de)intercalation during the early cycles. There are at least three different electrochemical processes before the Mg/FGS system reaches to the true reversible state. (1) The first charging is an initial activation process characterized by the insertion of ClO_4^- related anions. (2) The following second discharging is achieved by the insertion of Mg^{2+}-contained solvate cations (e.g., $Mg(DMSO)_nClO_4^+$) rather than anionic desorption. (3) The consequent second charging and deeper cycling are driven by the shuttle of cations likely consisting of $Mg(DMSO)_nClO_4^+$, $MgCl^+$, and $Mg_2Cl_3^+$. After initial cycles, the regular reaction equations at anode side can be expressed by

$$Mg(DMSO)_n ClO_4^+ + 2e^- \leftrightarrows Mg + n(DMSO) + ClO_4^- \tag{1}$$

$$MgCl^+ + 2e^- \leftrightarrows Mg + Cl^- \tag{2}$$

$$Mg_2Cl_3^+ + 4e^- \leftrightarrows 2Mg + 3Cl^- \tag{3}$$

and at cathode side by

$$\begin{aligned} &C - X(X = F, Cl, ClO_4) + Mg(DMSO)_n ClO_4^+ + 2e^- \\ &\leftrightarrows Mg - X - C + n(DMSO) + ClO_4^- \end{aligned} \tag{4}$$

$$C - X + MgCl^+ + 2e^- \leftrightarrows Mg - X - C + Cl^- \tag{5}$$

$$2C - X + Mg_2Cl_3^+ + 4e^- \leftrightarrows 2Mg - X - C + 3Cl^- \tag{6}$$

Previous reports on fluorinated graphite intuitively thought that Mg insertion into graphite interlayers and therein bonding with F groups are responsible for the considerable capacity.[11] Although in some cases the first charging was also resorted to, the importance of this process has not been well understood.[11b,c] Furthermore, the sluggish diffusion of Mg into graphite lattices usually results in large polarization, which is characterized by drastic voltage dropping at the starting of discharge followed by voltage climbing to a certain degree and then plateau formation at the main discharge stage.[11a,c] Insulating MgF_2 nucleation is likely responsible for the abnormal voltage dropping and then climbing during the early discharge. The plateau voltage (<1 V) is far lower than the thermodynamic equilibrium voltage of Mg/CF_x.[11a,22] Its average discharge voltage is 1.9 V lower than that for Li/CF_x, although their theoretical voltage difference referring to the formation of LiF and MgF_2 is only 0.6 V.

The combination of exposure of redox F sites, construction of mixed conductive networks, and first charge activation appears to a solution to the aforementioned kinetic and thermodynamic issues on multivalent ion storage. Electrochemical activation by the first charge is an anionic process and usually causes a higher reaction voltage (>1 V for most of the capacity in our case) due to modified reaction paths and corresponding difference in Gibbs free energy as demonstrated in early prototype of "dual-graphite cell."[8] Fluorinated ultrathin graphene instead of thick graphite is favorable to construct 3D porous frameworks with optimized mixed conductive networks and accessible redox sites. The observed symmetric charge/discharge curves and the absence of nucleation-induced voltage climbing mean a great improvement of polarization performance. Although the initial anionic activation complicates the following flowing of charge carriers, it appears to avoid undesired nucleation and growth of insulating MgF_2. Indeed, no large MgF_2 particles can be seen from the TEM of cycled samples (Figure 5), despite that the bonding of Mg—F has been confirmed. Compared with oxygenated graphene, additional fluorination is beneficial to the adsorption of ClO_4^--based anions (rather than Mg^{2+}-based cations), which serve as additional decoration groups to attract the arrival of Mg-contained cations accompanying a transformation of storage mechanism. Then more kinds of Mg-based cations participate in the following reversible cycling. The formation of complex always triggers the simultaneous motion of Mg and Cl, which is able to coordinate with Mg, dilute its charge density, and shield its electrostatic interaction with F. Indeed, these guarantee a facile formation and scission of Mg—F bonding (even though considering high ionicity of metal—fluoride bond) from the satisfactory reversibility. Otherwise, the Mg—F bonding is not easy to be broken as indicated in the primary Mg/CF_x battery without prior charge activation.[11a] The

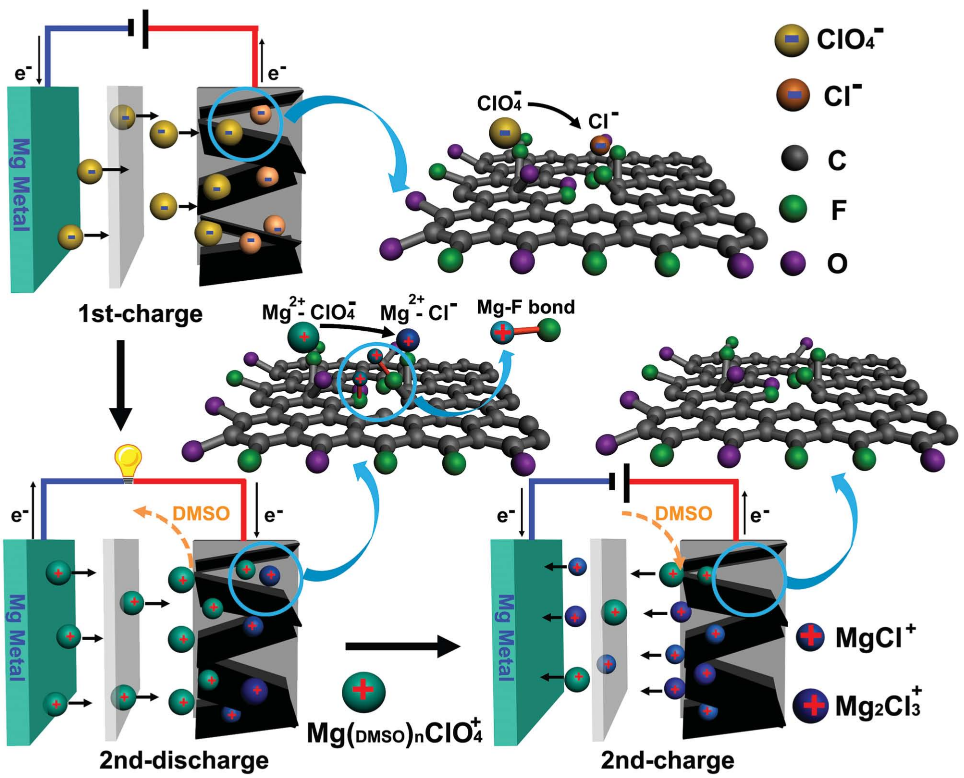

Figure 6. Scheme of electrochemical reaction mechanisms of a Mg/FGS battery involving multiple (complex) cation or anion (de)intercalations during the early cycles. 1) The first charging is an initial activation process characterized by the insertion of ClO_4^- related anions, a large fraction of which are converted to Cl^- based groups at the surface of carbon framework. 2) The following second discharging is achieved by the insertion of Mg^{2+}-containing solvate cations (e.g., $Mg(DMSO)_nClO_4^+$) rather than anionic desorption. The solvent molecules of DMSO are removed at the electrode–electrolyte interface before bonding of charge carriers with the carbon framework occurs, leading to the formation of potential interactions of Mg—F, Mg—ClO_4, and Mg—Cl. 3) The consequent second charging and deeper cycling are driven by the shuttle of cations likely consisting of $Mg(DMSO)_nClO_4^+$, $MgCl^+$, and $Mg_2Cl_3^+$. During the charging, DMSO molecules participate in the solvation process to form mobilizable $Mg(DMSO)_nClO_4^+$ again.

monovalent complex cations have faster migration rate than multivalent Mg^{2+} as seen from the good rate performance. The ultrathin electrode structure and surface reaction process allow XPS to a good tool to disclose the exact reaction mechanism. The FGS framework elements (e.g., C and F) show the opposite tendency on XPS peak intensity evolution to the migration cation (or anion) elements (e.g., Mg and Cl). The concentration increase or thicker covering of migration ions leads to a decrease of XPS peak intensity of FGS framework components, whereas the removal of migration ions results in the spectra recovering of FGS framework components. One should note that high salt concentration in Mg electrolyte (e.g., $Mg(ClO_4)_2$–DMSO system in this case) is crucial to guarantee the activity of Mg/FGS batteries, since anions are consumed during the first charging.

3. Conclusion

In summary, we reported a prototype of transition-metal-free magnesium-based battery activated by anionic insertion into fluorinated graphene nanosheets. Its advantages over traditional Mg/fluorinated graphite batteries lie in negligible voltage polarization between discharge and charge as well as pseudocapacitance-like reversible electrochemistry occurring at higher voltage. Such an Mg-storage performance benefits from surface reactions at accessible fluorinated functional groups of porous self-assembly conductive frameworks. Its cycling process is complicated by the conversion from anionic storage to cationic storage and the corresponding change of migration species. The charge density of Mg^{2+} is diluted by complexing with perchloride or chloride ions. These lead to a good reversibility and rate performance with a capacity of 110 and 90 mAh g^{-1} at 10 or 50 mA g^{-1}, respectively. This proof-of-concept system bypasses the sluggish diffusion of multivalent cations into the host lattice and structure distortion at the cathode, and it utilizes the fast occurrence of redox processes at surface decoration groups of ultrathin nanostructures in a common and cheap Mg-based nonaqueous electrolyte. This work paves the way to explore advanced multivalent storage systems coupled with safer anode and kinetically favorable cathode architectures.

4. Experimental Section

Preparation of FGSs: GO was chemically exfoliated from natural graphite flakes via a modified Hummer's method reported elsewhere.[23] FGSs were synthesized by a fluorination hydrothermal reaction. In a typical procedure, 40 mL of graphite oxide aqueous suspension (2.0 mg mL^{-1}) were put into a 50 mL Teflon-lined autoclave, where

0.5 mL HF (40 wt%, Shanghai Sinopharm Chemical Reagent Co.) was then added. The mixture was continuously sonicated to form a homogeneous suspension, and was then maintained at 180 °C for 30 h. After cooling to room temperature, the product was collected by filtering and washing with deionized water, and was finally dried through freeze-drying. For comparison, RGOs were also prepared by the similar steps and conditions for FGSs but without an addition of HF.

Structural Characterizations: The morphology and thickness of pristine FGSs (or cycled samples) were observed by TEM (JEOL JSM-6700F, operated at 200 kV) as well as scanning electron microscope (SEM, Magellan 400L, FEI) for STEM element mapping. The microstructures of GO, RGO, and FGS samples were analyzed by a X-ray diffractometer (D8 Discover, Bruker) in a 2θ range of 10°–80° at a scanning rate of 1.0° min^{-1} using Cu Kα radiation, as well as by Raman spectroscope (DXR Raman Microscope with 532 nm excitation length, Thermal Scientific Corporation). XPS measurements (ESCAlab-250) with an Al anode source were performed to characterize surface components and bondings of pristine RGO and FGS samples, as well as cycled FGS samples at different reaction stages.

Electrochemical Characterizations: Two-electrode coin 2025 cells were assembled in an argon-filled glove box (<0.1 ppm of water and oxygen). To prepare the working electrode, a mixture of FGS (or RGO), super-P, and SA (Alfa Aesar) with a weight ratio of 8:1:1 was pasted on the current collector of carbon paper. This as-fabricated electrode was dried in vacuum at 80 °C for 20 h. Mg foil (100–150 µm thick) was used as counter electrode. Both working and counter electrodes were electronically separated by a borosilicate glass-fiber sheet (Whatman GF/D). 0.75 M magnesium perchlorate ($MgClO_4$, Alfa Aesar, anhydrous) in anhydrous DMSO (Aldrich, ≥99.9%) was employed as Mg electrolyte. The charge–discharge tests of coin cells were carried out on the Land battery measurement system (CT2001A) with a voltage range of 0.5–2.75 V (or 0.5–2.5 V) versus Mg under different current densities from 10 to 100 mA g^{-1}. For both the Mg/FGS and Mg/RGO batteries, the initial discharge process is performed before the charge one in most cases. In fact, the following electrochemistry behavior does not depend on the initial discharge or charge. Even without a prior discharge process, the initial charge displays the similar voltage profile and capacity.

Supporting Information

Supporting Information is available from the Wiley Online Library or from the author.

Acknowledgements

This work was supported by the National Natural Science Foundation of China under Grant No. 51372263, by the China Postdoctoral Science Foundation under Grant No. 2014M561527, and by the Key Research Program of Chinese Academy of Sciences under Grant No. KGZD-EW-T06. C.L.L. would like to thank the supports from the "Hundred Talents" program of the Chinese Academy of Sciences and the Science Foundation for Young Researchers of State Key Laboratory of High Performance Ceramics and Superfine Microstructures.

Received: July 20, 2015
Revised: September 6, 2015
Published online: September 30, 2015

---

[1] J. Muldoon, C. B. Bucur, T. Gregory, *Chem. Rev.* **2014**, *114*, 11683.
[2] D. Aurbach, Z. Lu, A. Schechter, Y. Gofer, H. Gizbar, R. Turgeman, Y. Cohen, M. Moshkovich, E. Levi, *Nature* **2000**, *407*, 724.
[3] E. Levi, M. D. Levi, O. Chasid, D. Aurbach, *J. Electroceram.* **2009**, *22*, 13.
[4] a) R. G. Zhang, X. Q. Yu, K. W. Nam, C. Ling, T. S. Arthur, W. Song, A. M. Knapp, S. N. Ehrlich, X. Q. Yang, M. Matsui, *Electrochem. Commun.* **2012**, *23*, 110; b) M. M. Huie, D. C. Bock, E. S. Takeuchi, A. C. Marschilok, K. J. Takeuchi, *Coord. Chem. Rev.* **2015**, *287*, 15.
[5] a) C. Ling, D. Banerjee, W. Song, M. J. Zhang, M. Matsui, *J. Mater. Chem.* **2012**, *22*, 13517; b) Y. Orikasa, T. Masese, Y. Koyama, T. Mori, M. Hattori, K. Yamamoto, T. Okado, Z. D. Huang, T. Minato, C. Tassel, J. Kim, Y. Kobayashi, T. Abe, H. Kageyama, Y. Uchimoto, *Sci. Rep.* **2014**, *4*, 5622; c) M. Liu, Z. Q. Rong, R. Malik, P. Canepa, A. Jain, G. Ceder, K. A. Persson, *Energy Environ. Sci.* **2015**, *8*, 964; d) C. Kim, P. J. Phillips, B. Key, T. H. Yi, D. Nordlund, Y. S. Yu, R. D. Bayliss, S. D. Han, M. N. He, Z. C. Zhang, A. K. Burrell, R. F. Klie, J. Cabana, *Adv. Mater.* **2015**, *27*, 3377.
[6] O. Tutusaus, R. Mohtadi, *ChemElectroChem* **2015**, *2*, 51.
[7] a) S. Yagi, T. Ichitsubo, Y. Shirai, S. Yanai, T. Doi, K. Murase, E. Matsubara, *J. Mater. Chem. A* **2014**, *2*, 1144; b) Y. W. Cheng, Y. Y. Shao, J. G. Zhang, V. L. Sprenkle, J. Liu, G. S. Li, *Chem. Commun.* **2014**, *50*, 9644; c) S. J. Su, Z. G. Huang, Y. N. NuLi, F. Tuerxun, J. Yang, J. L. Wang, *Chem. Commun.* **2015**, *51*, 2641; d) N. Wu, Z. Z. Yang, H. R. Yao, Y. X. Yin, L. Gu, Y. G. Guo, *Angew. Chem. Int. Ed.* **2015**, *127*, 5849.
[8] S. Rothermel, P. Meister, G. Schmuelling, O. Fromm, H. W. Meyer, S. Nowak, M. Winter, T. Placke, *Energy Environ. Sci.* **2014**, *7*, 3412.
[9] a) R. G. Zhang, C. Ling, F. Mizuno, *Chem. Commun.* **2015**, *51*, 1487; b) X. Y. Zhao, Q. Li, Z. R. Zhao-Karger, P. Gao, K. Fink, X. D. Shen, M. Fichtner, *ACS Appl. Mater. Interfaces* **2014**, *6*, 10997.
[10] a) X. W. Cui, J. Chen, T. F. Wang, W. X. Chen, *Sci. Rep.* **2014**, *4*, 5310; b) S. W. Lee, N. Yabuuchi, B. M. Gallant, S. Chen, B. S. Kim, P. T. Hammond, Y. Shao-Horn, *Nat. Nanotechnol.* **2010**, *5*, 531; c) T. Y. Liu, R. Kavian, I. Kim, S. W. Lee, *J. Phys. Chem. Lett.* **2014**, *5*, 4324.
[11] a) J. Giraudet, D. Claves, K. Guerin, M. Dubois, A. Houdayer, F. Masin, A. Hamwi, *J. Power Sources* **2007**, *173*, 592; b) J. V. Rani, S. B. Rushi, V. Kanakaiah, S. Palaniappan, *J. Electrochem. Soc.* **2011**, *158*, A1031; c) V. Kanakaiah, M. Latha, B. Sravan, A. Palanisamy, J. V. Rani, *J. Electrochem. Soc.* **2014**, *161*, A1586.
[12] Z. F. Wang, J. Q. Wang, Z. P. Li, P. W. Gong, X. H. Liu, L. B. Zhang, J. F. Ren, H. G. Wang, S. R. Yang, *Carbon* **2012**, *50*, 5403.
[13] a) Y. X. Xu, K. X. Sheng, C. Li, G. Q. Shi, *ACS Nano* **2010**, *4*, 4324; b) Y. Zhou, Q. L. Bao, L. A. L. Tang, Y. L. Zhong, K. P. Loh, *Chem. Mater.* **2009**, *21*, 2950.
[14] K. Guerin, J. P. Pinheiro, M. Dubois, Z. Fawal, F. Masin, R. Yazami, A. Hamwi, *Chem. Mater.* **2004**, *16*, 1786.
[15] T. Shiga, Y. Hase, Y. Kato, M. Inoue, K. Takechi, *Chem. Commun.* **2013**, *49*, 9152.
[16] C. D. Wagner, *J. Electron Spectrosc. Relat. Phenom.* **1980**, *18*, 345.
[17] A. G. Wren, R. W. Phillips, C. U. Tolentino, *J. Colloid Interface Sci.* **1979**, *70*, 544.
[18] W. E. Morgan, J. R. Van Wazer, W. J. Stec, *J. Am. Chem. Soc.* **1973**, *95*, 751.
[19] W. J. Hunter, *Curr. Microbiol.* **2002**, *45*, 287.
[20] N. G. Gaylord, R. Mehta, V. Kumar, M. Tazi, *J. Appl. Polym. Sci.* **1989**, *38*, 359.
[21] a) J. A. Stone, T. Su, D. Vukomanovic, *Int. J. Mass Spectrom.* **2002**, *216*, 219; b) V. N. Agieienko, O. N. Kalugin, *J. Phys. Chem. B* **2014**, *118*, 12251; c) A. Migdał-Mikuli, E. Szostak, *Z. Naturforsch. A* **2005**, *60*, 289.
[22] a) C. X. Zu, H. Li, *Energy Environ. Sci.* **2011**, *4*, 2614; b) W. Liu, H. Li, J. Y. Xie, Z. W. Fu, *ACS Appl. Mater. Interfaces* **2014**, *6*, 2209.
[23] W. S. Hummers, R. E. Offeman, *J. Am. Chem. Soc.* **1958**, *80*, 1339.